AMERICAN
METEOROLOGICAL
SOCIETY

Journal of Physical Oceanography

EARLY ONLINE RELEASE

The DOI for this manuscript is doi: 10.1175/JPO-D-17-0017.1

The final published version of this manuscript will replace the preliminary version at the above DOI once it is available.

If you would like to cite this EOR in a separate work, please use the following full citation:

Lenain, L., and W. Melville, 2017: Measurements of the directional spectrum across the equilibrium-saturation ranges of wind-generated surface waves. J. Phys. Oceanogr. doi:10.1175/JPO-D-17-0017.1, in press.

Measurements of the directional spectrum across the equilibrium-saturation ranges of wind-generated surface waves

Luc Lenain* and W. Kendall Melville

Scripps Institution of Oceanography, La Jolla, California

**Corresponding author address:* Luc Lenain, Scripps Institution of Oceanography, 9500 Gilman Dr., La Jolla, CA 92093-0213.

E-mail: llenain@ucsd.edu

ABSTRACT

It is now well accepted that to better understand the coupling between the atmosphere and the ocean, and improve coupled ocean-atmosphere models, surface wave processes need to be taken into account. Here properties of the directional distributions of the surface wave field across the equilibrium-saturation ranges are investigated from airborne lidar data collected during the ONR SOCAL2013 experiment, conducted off the coast of Southern California in November 2013. During the field effort, detailed characterization of the marine atmospheric boundary layer was performed from R/P FLIP, moored at the center of the aircraft operational domain. The wind speed ranged from approximately 1-2 m/s to up to 11 m/s while the significant wave height varied from 0.8 to 2.5m during the 10 days of data collection considered in the analysis. The directional wavenumber spectrum exhibits a clear bimodal distribution that extends well beyond what was reported in previous studies, with the azimuthal separation between the lobes reaching $\approx \pi$ for the highest wavenumbers we could resolve: approximately 10-12 rad/m. The results demonstrate that opposing wave components can be found in one storm system rather than requiring waves from opposing storms, with implications for ocean acoustics. With the broad wavenumber range of the directional spectra obtained from the lidar, the transition from the equilibrium to saturation ranges over a range of wind forcing conditions is found to occur for $k_n u_*^2/g \approx 1-2\times10^{-3}$. The results are discussed in the context of Phillips' (1985) model of the equilibrium range of wind-generated gravity waves.

1. Introduction

Over the last several decades, there has been growing recognition from both oceanographic and atmospheric sciences communities that surface waves play a crucial role in the processes by which the ocean and atmosphere interact.

Until recently, most of the observational literature on surface waves was driven by studies based on time series of wave measurements at a point (or at a relatively slowly-moving mooring) combined with directional information from the dynamics of the moving (pitch-roll) buoy or measurement platform. The directional and frequency response of these systems is limited and not capable of the resolution required to fully test modern theories of directional surface-wave spectra. Additionally, Doppler shift induced by longer dominant waves can distort the high frequency portion of wave frequency spectra (Kitaigordskii et al. 1975; Banner 1990).

It is only in the last two decades that observations of bimodal directional spectra at wavenumbers and frequencies higher than the spectral peak have been available to test numerical predictions (Banner and Young 1994; Dysthe et al. 2003; Romero and Melville 2010b; Romero et al. 2012). However, these observations are typically limited to wavenumbers and frequencies that are just a few multiples of the peak values (Hwang et al. 2000a,b; Romero and Melville 2010a); most recently up to 25 times the peak wavenumber (Leckler et al. 2015). Directional observations at higher wavenumbers, those approaching wavelengths at the lower end of the gravity-wave range, are especially limited, but are important as the spectrum transitions into the shorter wavelengths that are of direct relevance for many aspects of air-sea interaction and the interpretation of many remote sensing techniques. Recent improvements in image processing techniques have lead to significant progress in our ability to better understand the spatio-temporal properties of short gravity waves, through stereo imagery (Leckler et al. 2015; Yurovskaya et al. 2013) or polarimetric techniques (Zappa et al. 2008), but these studies are generally limited to wavelengths shorter than a few meters, due to the small field of view generally considered. Also they are potentially affected by wave reflections from the platform or ship from which the measurements are collected.

Here we focus on directional wavenumber measurements of the surface-wave field extending from kilometer down to submeter scales using airborne topographic lidar. In recent years, the development of scanning lidars along with high-precision GPS and inertial motion units (GPS/IMU) has permitted airborne measurements of the sea surface elevation with swath widths of order 100 to 1000 m under the aircraft track (Hwang et al. 2000a; Romero and Melville 2010a; Reineman et al. 2009; Melville et al. 2016), significantly improving our understanding of the physical regimes occurring over a broader range of wave scales.

The omnidirectional wavenumber spectrum $\Phi(k)$, where k is the wavenumber, computed by integrating azimuthally a directional wavenumber spectrum, $\phi(k,\theta)$, is traditionally described by a peak wavenumber, followed by a region approximately proportional to $k^{-5/2}$, or its frequency equivalent [1], ω^{-4}, where ω is the radial frequency, referred to as the *equilibrium* range. This region of the wave spectrum has been extensively studied, both through analytical, spatial and temporal observations (Donelan et al. 1985; Battjes et al. 1987; Hwang et al. 2000a; Romero and Melville 2010a; Melville et al. 2016, among others) and numerical investigation (Pushkarev et al. 2003; Romero and Melville 2010b, among others) of the wave field, more specifically of wind waves. Kitaigorodskii (1983), largely based on the pioneering work of Phillips (1958) and Kitaigorodskii (1962), suggested that the spectral form of the equilibrium range of the wind-wave spectrum was the direct consequence of a Kolmogoroff-type energy cascade from low to high frequency, combined with the existence of gravitational instabilities (breaking waves). Zakharov and Filonenko (1967) found a similar spectral shape by deriving a "wave turbulence" Kolmogoroff-

[1] based on the deep water dispersion relationship

type solution based on resonant interactions between weakly nonlinear surface gravity waves. In 1985, Phillips proposed a model of the equilibrium range, built around the assumption that the nonlinear energy flux, wind forcing and energy dissipation from breaking waves are in *balance*, *proportional*, and of *similar magnitude* (Phillips 1985). His model also predicts a $k^{-5/2}$ spectral shape for the equilibrium range. It should also be noted that empirical parameterizations of this spectral region are also available (Toba 1973; Resio et al. 2004).

Beyond the equilibrium range, spatial and temporal observations of wind waves as well as numerical studies show a power law transition from a $k^{-5/2}$ to a k^{-3} slope (Forristall 1981; Banner 1990; Romero and Melville 2010a,b; Romero et al. 2012), corresponding to another regime, the *saturation* range. Here, the primary balance is between the wind input and the dissipation from breaking waves. Observational evidences of the transition between the equilibrium and saturation ranges are very limited, as a broadband wavenumber spectrum is needed to fully resolve both regimes.

In the present study, we investigate the properties of directional wavenumber spectra of surface gravity waves, including the transition from equilibrium to saturation ranges, collected in November 2013 off the coast of California from an airborne scanning lidar installed on a research aircraft. The experiment, instrumentation, environmental conditions and processing techniques are presented in section 2. Section 3 describes the directional properties of the wave field, including bi-modality, the transition from the equilibrium to the saturation ranges, and provides some insight on the contribution of the equilibrium range to the mean square slope, $\langle s^2 \rangle$, in the context of the seminal work of Cox and Munk (1954). Results are summarized in section 4.

2. Experiment

Data were collected during the SOCAL2013 experiment, an Office of Naval Research (ONR) funded project specifically designed to collect spatio-temporal, phased-resolved measurements of wind and waves over a broad range of environmental conditions. The experiment was located between San Clemente and San Nicholas Islands ($33^{o}13.202'$N,$118^{o}58.767'$W) where R/P FLIP was moored, from November 7 to 22, 2013. R/P FLIP was instrumented with a suite of sensors described below to characterize the atmospheric, surface and subsurface conditions at the experiment site. A total of 7 research flights are considered in the analysis, corresponding to 19.2 hrs on station.

a. Sea Surface Topography

Spatio-temporal measurements of the sea surface topography and surface kinematics were collected from a Partenavia P68 aircraft instrumented with the Modular Aerial Sensing System (MASS), an instrument package developed at Scripps Institution of Oceanography (SIO) (Melville et al. 2016).

At the heart of the system, and of specific interest for this study, a Q680i waveform scanning lidar (Riegl, Austria) is used to make spatio-temporal measurements of the sea surface. The sensor has a maximum pulse repetition rate of 400 kHz, a maximum $\pm 30^{\circ}$ cross-heading raster scan rate of 200Hz, and has been used at altitudes up to 1500 m with good returns for surface-wave measurements. The theoretical swath width over water is typically proportional to the altitude of the aircraft[2], and its effective width is also dependent on the wind speed and sea state. More details are available in Melville et al. (2016) and Reineman et al. (2009), the latter presenting detailed performance analysis from an earlier version of the MASS.

[2]The swath width is close to the aircraft altitude.

The MASS is also equipped with a 14-bit, 640x512 QWIP FLIR SC6000 infrared camera operating up to a 126 Hz frame rate in the 8.0-9.2 μm band, to measure the ocean surface temperature field including modulations and gradients due to fronts, surface signatures of Langmuir circulation and wave breaking (Sutherland and Melville 2013). A hyperspectral camera (SPECIM AisaEagle, Finland) operating in the 400-990 nm range (visible to near-IR) and a JaiPulnix (San Jose, CA USA) AB-800CL (3296px x 2472px) color (24 bit) video camera that operates at a frame rate up to 17 Hz are used to provide visible imagery of the kinematics of whitecaps (Melville and Matusov 2002; Kleiss and Melville 2010, 2011; Sutherland and Melville 2013).

All data collected are carefully georeferenced from the aircraft to an earth coordinate frame using a Novatel SPAN-LN200; a very accurate GPS-IMU system combining GPS technology with an IMU using fiber-optic gyros and solid-state accelerometers to provide position and attitude data at up to 200 Hz. After differential GPS processing, using Waypoint Inertial Explorer software (Novatel Inc.), the stated accuracy for the instrument position is 0.01 m horizontal and 0.015 m (vertical), with attitude accuracies of 0.005°, 0.005°, and 0.008° for roll, pitch, and heading, respectively. A calibration-validation flight is conducted prior to and after each campaign to minimize boresight errors due to the misalignment between the GPS-IMU system and the lidar (Melville et al. 2016). Once calibrated, we typically find absolute vertical errors for the topographic product of 2 to 4 cm (per ping), estimated at 2.3 cm in the present study from the calibration flight conducted prior to and after the experiment.

b. Environmental conditions

A suite of atmospheric sensors was installed on R/P FLIP's port boom to characterize the marine atmospheric boundary layer variables used in the analysis. Wind speed and direction were measured using an array of five sonic anemometers (four CSAT3 and one Gill R3-50) mounted on a vertical telescopic mast that was deployed from the end of the port boom of FLIP, ranging from approximately 15 down to 2.65 m above mean sea level (AMSL). The altitude above mean sea level varied during the course of the experiment, depending on environmental conditions (Grare et al. 2016) but were typically in the range of 2.6 to 4 m AMSL, for the lowest sensor, the Gill R3-50. The friction velocity in the air, u_*, is given by

$$u_* = (\overline{u'w'}^2 + \overline{v'w'}^2)^{1/4} \tag{1}$$

where the covariances $\overline{u'w'}$ and $\overline{v'w'}$ are computed over 30-min records from the average cospectra for (u', w') and (v', w').

The Gill sonic anemometer was preferred over the Campbell model to compute the friction velocity, following the recommendations of Grare et al. (2016) who demonstrated the better performances of this unit in varying wind directions. Nevertheless, we found that during the research flights, all five sensors show consistent atmospheric friction velocity values, within $5-10\%$, implying that the measurements were collected in a constant stress layer. The wind speed at 10-m height, U_{10}, was interpolated between the data collected at the closest measurement heights, approximately 8.5 m and 14.5 m AMSL, assuming a constant flux layer with a logarithmic wind profile.

Figure 1(a) shows the time series of wind speed U_{10} in m/s and corresponding wind direction for the duration of the R/P FLIP deployment. Figure 1(d) shows the friction velocity u_* also in m/s for the same period of time. Note the gray areas corresponding to the times when the aircraft was collecting data in close proximity (i.e. $<$10km) to R/P FLIP. The wind speed, particularly variable over the duration of the experiment, ranged from approximately 1-2 m/s to up to 11 m/s. In addition, an array of five nadir-looking laser wave gauges (MDL ILM500), located on the three booms of FLIP, was used to sample the directional frequency spectrum of the sea surface elevation. All wave time series were corrected for FLIP's motion using a state of the art GPS-IMU: a Novatel SPAN-CPT mounted on the port boom. Figure 1(b) shows the spectrogram of the sea surface displacement computed for one of the wave gauges installed on the port boom. A series of short local wind events can be clearly seen, with peak energy slowly moving toward the lower frequency as the waves grow. The significant wave height, H_s, is shown in figure 1(c), ranging from 0.8 to up to 2.5m on November 16, 2013. The amplitude of the swell component in the spectra was found to be typically 1 to 2 orders of magnitude lower than the wind component. In the few cases considered in the analysis where the spectral amplitude of the swell component was larger than that of the wind, the swell and wind seas were approximately aligned.

c. Spectral analysis

Surface elevation data collected from the MASS lidar were carefully georeferenced from aircraft to an earth-coordinate 3D point cloud. Ten-kilometer long swaths of data centered on R/P FLIP were gridded and interpolated on a regular grid, with the horizontal spatial resolution a function of the flight altitude: $dx = dy = 0.1m$ for aircraft altitude lower than 200m AMSL (typical swath width 50-150m), and $dx = dy = 1m$ for higher altitude (typical swath width of 200-800m). The data collected at the edge of the swath were discarded due to high dropout rates ($<$10-15% returns). Two-dimensional Fast Fourier Transforms were computed over 5km segments with 50% overlap. All segments were first detrended, tapered with a two-dimensional Hanning window and padded with zeros (25%). To correct for the Doppler shift induced by the relative motion between the phase speed of the wave and the aircraft velocity, each spectrum was corrected iteratively following the method developed by Walsh et al. (1985). The change in wavenumber component in the along track direction is taken as

$$\delta k_x = \frac{\omega}{v_a} \tag{2}$$

where $\omega(k)$ (rad/s) is the radial wave frequency, computed from a deep-water dispersion relationship, and v_a (m/s) is the aircraft velocity in the along-track-direction.

d. Wind-wave modelling

Identifying the upper wavenumber limit of the equilibrium range (Phillips 1985) is of obvious importance for wave modelling. Romero and Melville (2010b) and Romero et al. (2012) empirically defined this upper limit as a function of the zero-up crossing, k_u, of the azimuth-integrated non-linear energy fluxes based on the requirements of Phillips 1985's equilibrium model. In particular, Phillips requirement that all three "source" terms be proportional excludes zero crossings if any one term is sign-definite, as is dissipation. The present data set offers an unique opportunity to test this assumption, as the measured directional wavenumber spectrum extends from the equilibrium into the saturation range. Here, the non-linear wave-wave interaction source function, S_{nl}, is computed from the measured wave directional spectrum $\phi(k,\theta)$ using the so-called exact Webb-Resio-Tracy (WRT) method by Tracy and Resio (1982), based on the work by Webb (1978). We used the implementation from van Vledder (2006) used in WAVEWATCH III. Note that an αk^{-4} spectral tail (α a constant) was added to the directional spectrum for wavenumber, k, larger than k_m, the wavenumber corresponding to the measured noise floor, following the methodology described in Romero et al. (2012).

3. Results

a. Bimodal structure of the directional wave spectrum

An example of a directional spectrum $\phi(k,\theta)$ from a flight conducted on November 15, 2013, is shown in Figure 2. These data down to wavelengths of approximately 50 cm were acquired at a flight altitude of approximately 200m. For clarity, two versions of the same directional spectrum are shown (a) in linear wavenumber scale, only extending to 2 rad/m to highlight the bimodal distribution and (b) a logarithmic wavenumber scale plot showing the full wavenumber range of the measured spectrum, extending over almost 3 decades, up to 12 rad/m . The wind speed, U_{10}, collected from R/P FLIP was equal to 10.2 m/s at the time of the measurements.

The bimodal distribution of the directional wave spectrum for wavenumbers larger than the spectral peak has been measured in a number of past studies (Hwang et al. 2000b; Long and Resio 2007; Romero and Melville 2010a; Young 2010). Romero and Melville (2010a) found the bimodal distribution to extend out to 4-5 times the peak wavenumber k_p, but were limited by the horizontal sampling resolution of the lidar they used. Similar results from a stereo imaging system installed on the Katsiveli platform (Black Sea coast of Crimea) were found recently by Leckler et al. (2015) where measurements of the bimodal distribution extended up to $k/k_p \approx 25$. In the present study, we find bimodal distributions extending up to $k/k_p \approx 100$, as shown in Figure 3, where the directional spectrum $\phi(k,\theta)$ is plotted against normalized azimuthal direction $\theta-\theta_p$, where θ_p is the peak direction. Here $k_p = 0.024\ rad/m$,while the bimodal peaks reach approximately $\pm\ 90^o$ at a wavenumber of approximately 3-4 rad/m and remain weakly bimodal for higher wavenumbers. To our knowledge, these are the first directional wave spectrum measurements over such a broad range of scales. We define the half azimuthal separation between the two lobes as

$$\theta_{lobe}(k) = \frac{|\theta_1 - \theta_2|}{2}, \tag{3}$$

where $\theta_1(k)$ and $\theta_2(k)$ are the azimuthal angles corresponding to the two maxima of the bimodal distribution.

Figure 4 shows the azimuthal separation $\theta_{lobe}(k)$ colorcoded for wave age, equal to c_p/u_*, where c_p is the peak phase velocity, as a function of k/k_p and the non-dimensional wavenumber $\hat{k} = ku_*^2/g$, following Phillips (1985) scaling of the upper limit of the equilibrium range (top and bottom panels respectively). Also shown are the measurements by Hwang et al. (2000b) (black triangle). Data from the GOTEX experiment (see Romero and Melville 2010a, for details) are also plotted as solid lines with open circles.

While we find a lot of scatter in figure 4(a), the collapse of the data in (b) is remarkable. Here we fit the data over that range to the functional form

$$\theta_{lobe} = \theta_o + \gamma log(\hat{k}) \tag{4}$$

with $\theta_0 = 2.835$ and $\gamma = 0.48$ ($r^2 = 0.96$), valid over the range $3 \times 10^{-3} < \hat{k} < 6 \times 10^{-2}$. The directional resolution of the bifurcation from a unimodal to a bimodal distribution in the neighborhood of $\hat{k} = 3 \times 10^{-3}$ and to $\theta_{lobe} = \pi/2$ in the neighborhood of $\hat{k} = 6 \times 10^{-2}$ is not sufficient to posit a functional form resolving these areas.

The lack of collapse of the azimuthal separation plotted against k/k_p is likely associated with other processes involved in the evolution of the longer wavelength portion of the spectrum (e.g. non-linear wave-wave interactions) and measurement errors in estimating k_p.[3]

Also recall that the cross-track swath width is much shorter than the along-track, effectively reducing the azimuthal directional resolution $d\theta$ we can achieve for the longer waves of our spectra. Following Romero and Melville (2010a), we compute $d\theta$ as

$$d\theta = \frac{dk_2}{k}, \tag{5}$$

where dk_2 is the spectral resolution in the cross-track direction. Values of $d\theta$ for representative wavenumbers are shown in table 1. The lack of sufficient directional resolution for the lowest wavenumbers, i.e. $\hat{k} < 2 - 4 \times 10^{-3}$ makes the identification of a bimodal distribution for this range of wavenumbers particularly difficult.

[3] The horizontal offset is driven by k_p.

Overall, we find that the half azimuthal separation extends well beyond what was reported in previous studies, reaching close to $\pi/2$ for the highest wavenumbers, right at the limit of what we can azimuthally resolve in the present data set. This effectively implies that waves propagating in opposing directions can be found at scales of wavenumbers around 10-12 rad/m, or 10-11 rad/s for linear gravity waves in the frequency domain. The existence of such wave systems has been argued to be a leading mechanism through which microseismic noise is generated (Longuet-Higgins 1950; Ardhuin et al. 2015). Space-time measurements of the evolution of the wave field are needed to explore this topic further.

The average amplitude of the lobes relative to the spectral energy in the dominant wave direction $r_{lobe}(k)$ is defined as

$$r_{lobe}(k) = \frac{\phi(k,\theta_1)+\phi(k,\theta_2)}{2\phi(k,0)}. \tag{6}$$

Figure 5(a) shows the measured $r_{lobe}(k/k_p)$ colorcoded for wave age for the SOCAL2013 (solid line) and GOTEX (solid line with circle) experiments. The black open triangle corresponds to the measurements by Hwang et al. (2000b). We find that r_{lobe} generally increases as a function of k/k_p, reaching $r_{lobe} \approx 2$, with a few cases showing an amplitude reduction after reaching the maxima.

Figure 5(b) shows $r_{lobe}(k)$ for the SOCAL2013 (solid line) and GOTEX (solid line with circle) experiments colorcoded for wave age, plotted against $\hat{k} = ku_*^2/g$. The set of curves we obtain are better collapsed than in Figure 5(a), but more work is needed to explain the remaining scatter.

b. Azimuthally integrated wave spectrum properties

Figure 6 shows the azimuthally integrated omnidirectional spectrum computed from the directional spectrum presented in figure 2. The separation at wavenumber k_n of the spectral slopes into -2.5 (equilibrium) and -3 (saturation) regions is clear with $k_n = 0.6$ rad/m in this specific example. The first region corresponds to the equilibrium range while the second is traditionally referred to as the saturation range (e.g. Banner et al. 1989; Banner 1990; Hwang et al. 2000a,b; Romero and Melville 2010a). Phillips (1985) proposed a model of the equilibrium range, based on the assumption of balance, proportionality and similar order of magnitude of the terms in the radiative transfer equation, namely the wave-wave interactions, wind forcing and wave-breaking dissipation. His model, and others, predicts a $k^{-5/2}$ slope for the equilibrium range of the omnidirectional spectrum, in agreement with the present measurements.

Figure 7 shows the frequency spectrum computed from a nadir looking lidar altimeter installed on FLIP's port boom at the same time and location the airborne lidar data shown in figure 6 were collected. The equilibrium and saturation ranges identified from the wavenumber spectrum are shown in red and blue, for reference, as well as the peak and transition frequencies, f_p and f_n, computed from k_p and k_n, assuming the deep-water dispersion relationship. While the transition is obvious in the wavenumber spectrum, the frequency spectrum does not exhibit any clear change of slope between the two regimes.

Temporal point measurements are more likely to be influenced by the Doppler shift caused by the orbital motions of longer waves on the shorter waves (Kitaigordskii et al. 1975; Banner 1990). A vertical gradient of horizontal velocity close to the surface leads to Doppler effects of varying amplitude as a function of frequency (i.e. penetration depth), and therefore has the potential to change the slope of the wave frequency spectrum. Additionally, frequency spectra measured from single point wave gauges or buoys are generally noisier, making it harder to identify slope behavior. To illustrate this effect, we also show in figure 7 the frequency spectrum computed from the measured directional wavenumber spectrum (gray solid line) assuming the deep-water dispersion relationship, following Phillips (1985), where the frequency spectrum $S(\omega)$ is defined as

$$S(\omega) = 2g^{-1/2} \int_{-\pi}^{\pi} \left[k^{3/2} \phi(k, \theta) \right]_{k=\omega^2/g} d\theta. \tag{7}$$

This time the transition from a f^{-4} to f^{-5} power law is evident. This result reiterates the more fundamental nature of the spatial measurements of the wave field for elucidating the dynamics, as compared to the traditional parameterization of the wave field based on single point, temporal measurements from wave gauges or buoys.

Figure 8 shows wavenumber omnidirectional spectra colorcoded for $u_*/\sqrt{gH_s}$ collected during the SOCAL experiment. The term $u_*/\sqrt{gH_s}$ is a non-dimensional quantity corresponding to the atmospheric friction velocity scaled by the velocity $\sqrt{gH_s}$, the speed at impact of a particle following a ballistic trajectory from a height $H_s/2$. This quantity has been used to parameterize wave breaking dissipation (Drazen et al. 2008), whitecap coverage (Sutherland and Melville 2013) and more recently air entrainment by breaking waves (Deike et al. 2017). This definition was preferred to the more traditionally used wave age, equal to c_p/u_*, as c_p, the peak phase velocity, is often difficult to characterize, especially in the conditions we experienced during the experiment (a mix of swell and wind waves coming from multiple directions). Also note that in fetch limited conditions, $c_p \propto \sqrt{gH_s}$.

We find that as $u_*/\sqrt{gH_s}$ increases, the transition between equilibrium and saturation ranges is reached at lower wavenumbers, as Phillips suggested for decreasing wave age (Phillips 1985).

c. Scaling of the saturation spectrum by the friction velocity

We introduce the azimuth-integrated saturation spectrum, $B(k)$, defined as

$$B(k) = \int \phi k^4 d\theta. \tag{8}$$

The saturation spectra $B(k)$, colorcoded for $u_*/\sqrt{gH_s}$, computed from the directional wave spectra collected during the experiment are shown in Figure 9. Spectral levels in the equilibrium and saturation ranges are increasing as a function of $u_*/\sqrt{gH_s}$, converging to a constant saturation level around 7 rad/m then increasing for the highest wavenumbers, up to 12-13 rad/m. This level increase beyond 7 rad/m could be physical as other studies have predicted an increase of the saturation level for this range of wavenumbers. However, since it is also near the limit of the spatial resolution of the measurements it could also be measurement noise. A subset of these saturation spectra is shown in figure 10, this time colorcoded for the wind speed, U_{10}, to compare the spectral saturation levels to past studies and numerical parameterization of the *omnidirectional* saturation spectrum. Here we show results from stereo-imagery field measurements (Banner et al. 1989; Yurovskaya et al. 2013, Veron et al. 2017, manuscript in preparation), imaging slope gauge data collected in a laboratory experiment (Jähne and Riemer 1990), an empirical formulation based on field measurements from a wave gauge array (Hwang 2005) and numerical parameterization (Elfouhaily et al. 1997). While we find a lot of scatter between all these studies, the spectral levels found in the present study are generally within the range of other data sets. The equilibrium range levels are consistent with the Elfouhaily et al. (1997) model for the larger wind speeds and Hwang (2005) for the intermediate wind speeds ($U_{10} = 5.8$ m/s). The spectral levels in the saturation range are within the scatter of the other studies. Note the increase in B found for $k > 7\ rad/m$, stressing the need for field measurements of saturation spectra at higher wavenumbers.

The saturation spectra presented in figure 9 are shown in figure 11, also colorcoded for $u_*/\sqrt{gH_s}$, but this time as a function of the non-dimensional wavenumber $\hat{k}$, following Phillips (1985) scaling of the upper limit of the equilibrium range. He defines

$$k_n = rg/u_*^2, \tag{9}$$

where r is a constant [4]. The saturation spectra collapse for non-dimensional wavenumbers $\hat{k}$ above 2×10^{-3}, both in the equilibrium ($\hat{k}^{-1/2}$, extending to $\hat{k} \approx 10^{-2}$) and saturation ranges. The transition wavenumber, k_n, is computed for each saturation spectrum, estimating the intersect between a $k^{-1/2}$ fit in the equilibrium range and a constant saturation value at higher wavenumbers.

Figure 12 shows k_n plotted against $u_*/\sqrt{gH_s}$, along with a quadratic fit of the data that gives

$$k_n = \Gamma_1 \left(u_*/\sqrt{gH_s}\right)^2 - \Gamma_2 \left(u_*/\sqrt{gH_s}\right) + \Gamma_3 \tag{10}$$

where $\Gamma_1 = 1.7 \times 10^3$, $\Gamma_2 = -3.3 \times 10^2$, and $\Gamma_3 = 18$ ($r^2 = 0.94$).

We introduce here the non-dimensional fetch χ^*, computed from the empirical formulation of Kahma and Calkoen (1992):

$$\chi^* = g\chi/u_*^2, \tag{11}$$

where χ is the fetch. Using the unstable stratification formulation based on the dimensionless peak frequency $\omega_p^* = 2\pi f_p u_*/g$,

$$\omega_p^* = 3.755\,(\chi^*)^{-0.287}. \tag{12}$$

Eddy flux measurements collected on R/P FLIP (Grare et al. 2017, manuscript in preparation), showed the atmosphere to be unstable at the time and location where the data were collected.

We find r to vary between 0.01 and 0.025, a factor of 2.5, over the range of wave ages experienced during the field effort (Figure 13), $30 < c_p/u_* < 120$. The term r remains also approximately constant as a function of non-dimensional fetch. Since identifying an appropriate phase speed, c_p, is challenging and typically requires strong assumptions, c_p is computed in two ways: from the in-situ lidar measurements collected on R/P FLIP based on the wind-wave frequency spectrum peak (labeled as "wind waves only") and from the peak frequency (labeled as "full spectrum").

[4] r is assumed constant for fully developed seas in Phillips (1985)

d. Non-linear energy fluxes in equilibrium and saturation ranges

The non-linear term S_{nl} of the radiative transport equation was computed from the measured directional wavenumber spectra assimilated into WaveWatch III using the implementation from van Vledder (2006). An example is shown in figure 14. The black arrow in the figure corresponds to the direction the waves are *propagating*. S_{nl} is positive over the measured range of azimuth and wavenumber, but in the peak direction of wave propagation, for $k \approx 1-4\times10^{-1}$, S_{nl} is found to be negative. Along the same direction, for lower and higher wavenumbers, the same term is positive. The evolution of S_{nl} is consistent with the work of Romero and Melville (2010a) and Romero et al. (2012), where k_n was defined as a function of the zero-up crossing k_u of the azimuth-integrated non-linear energy fluxes S_{nl}. This was motivated in part by Phillips' (1985) equilibrium argument, which by assuming that the three source terms were all proportional can not include zero crossings in the nonlinear term since the wind input, under Phillips assumptions, was positive definite [5]. Figure 15 shows k_n plotted against its corresponding k_u, colorcoded for u_*. Two reference dashed lines are also shown, in blue, $k_n = 2k_u$, and in gray $k_n = k_u$. For larger values of u_*, k_n is close to twice the zero-up crossing wavenumber, decreasing to a range between 1-2 $\times k_u$ as u_* decreases below 0.3 m/s.

The dependence of the ratio k_n/k_u over wave age is shown in Figure 16(a). Here the wave age is computed using the peak wavenumber k_p. We find that the ratio is decreasing with wave age. A quadratic fit of the data gives:

$$\frac{k_n}{k_u} = a_1\left(\frac{c_p}{u_*}\right)^2 + a_2\left(\frac{c_p}{u_*}\right) + a_3, \tag{13}$$

where $a_1 = 1.36\times10^{-4}$, $a_2 = -2.89\times10^{-2}$, and $a_3 = 2.43$.

[5] If considering swell as well as wind waves, then the wind input term can be negative since momentum can be transferred from the waves to the wind (Hanley et al. 2010).

As mentioned in earlier sections, correctly identifying c_p is particularly challenging and might be misleading when the spectral peak wavenumber k_p is used. Figure 16(b) shows the dependence of the ratio k_n/k_u on the non-dimensional quantity $u_*/\sqrt{gH_s}$. We find that the ratio is increasing with $u_*/\sqrt{gH_s}$. An exponential fit[6] of the data gives:

$$\frac{k_n}{k_u} = b_1 + b_2 e^{\frac{b_3 u_*}{\sqrt{gH_s}}}, \tag{14}$$

where $b_1 = 9.3 \times 10^{-1}$, $b_2 = 4.0 \times 10^{-4}$, and $b_3 = 84.4$.

e. Contribution from the equilibrium range to the total mean-square slope

In deriving the total mean-square slope associated with the equilibrium range, Phillips (1985) showed that r, the constant used in his study to relate k_n to u_*, is defined as

$$r = \frac{\left\langle s^2 \right\rangle^2}{\beta^2} \tag{15}$$

where $\left\langle s^2 \right\rangle$ is the total mean-square slope computed over the equilibrium range, from k_o to k_n, and β is Toba's constant. Here β is computed from the equilibrium range of the omnidirectional wave spectrum following Toba (1973), where the equilibrium range is defined as

$$\Phi(k) = \frac{\beta}{2} u_* g^{-1/2} k^{-5/2}. \tag{16}$$

Toba's constant β is calculated here as

$$\beta = \frac{2g^{1/2}}{u_*} \left\langle \Phi(k) k^{5/2} \right\rangle \tag{17}$$

where the mean compensated spectrum $\left\langle \Phi(k) k^{5/2} \right\rangle$ is computed over the equilibrium range, integrated from $2.25k_p$ to k_n. The low wavenumber bound was set according to Donelan et al. (1985), also used in Romero and Melville (2010a), to avoid contamination from the spectral peak.

[6]We found a better r^2 using an exponential growth fit as opposed to a quadratic fit, 0.84 and 0.76 respectively, which motivated its use.

Figure 17 shows r computed from equations 9 and 15. We obtain values ranging from 0.01 to 0.025 using equation 9 and generally lower values using equation 15, ranging from 0.005 to 0.015. Using the limited observational data available at the time, Phillips concluded that $r \approx 0.3$, a value much larger than what we find in the present study. This discrepancy is not unexpected, and caused by the fact that Phillips used Cox and Munk's (1956) classical result to compute the total mean-squared slope. Their estimate, derived from airborne measurements of sunglitter, does not discriminate between equilibrium and saturation ranges. The saturation range, and beyond, in the capillary range, contributes significantly to the mean-square slope, in turn, leading to significant overestimation of r in Phillips' work.

In Figure 18 we characterize the contribution of the equilibrium range to the total mean-square slope. The term $\left\langle s^2 \right\rangle(k)$ is computed cumulatively based on the measured directional wave spectrum, defined as

$$\left\langle s^2 \right\rangle(k) = \int_{k_o}^{k} S(m)dm \tag{18}$$

where

$$S(k) = \Phi(k)k^2. \tag{19}$$

As our reference, we use here the classical parameterization from Cox and Munk (1954), subsequently confirmed by Bréon and Henriot (2006), that

$$\left\langle s^2 \right\rangle_{ref} = s_a + s_b U_{10} \pm \varepsilon, \tag{20}$$

where $s_a = 4 \times 10^{-3}$, $s_b = 5.01 \times 10^{-3}$ and $\varepsilon = 0.71 \times 10^{-3}$. Note that U_{10} was estimated from satellite scatterometry in Bréon and Henriot (2006), while the wind speed in Cox and Munk (1954) was measured from an anemometer installed 12.5m above the deck of a sailboat located at the experiment site. Each curve is colorcoded for friction velocity. We find that the contribution from the equilibrium range typically corresponds to just $10-30\%$ of the total mean-square slope.

4. Summary and discussion

Detailed topographic measurements of surface waves, ranging from kilometer to submeter scales, collected from an airborne, scanning, high-resolution waveform lidar, combined with in-situ marine atmospheric boundary layer data recorded on R/P FLIP during the ONR SOCAL2013 experiment, has provided an opportunity to characterize the directional properties of the wave field across the equilibrium-saturation ranges of wind-generated surface waves and correlate them with the wind forcing. To our knowledge, this is the first study that shows directional characterization of surface waves over such a broad range of wavenumbers and environmental conditions (i.e. wind forcing).

Our measurements extends the known bimodal distribution well beyond what was reported in previous studies, with an azimuthal separation between the two lobes reaching close to π for the highest wavenumbers we could resolve, up to $k/k_p \approx 100-200$. Though more work is needed, in particular to resolve the 180^o ambiguity in the directional spectrum computed from the lidar topographic surface wave maps, these results show that waves propagating in opposing directions can be found at wavenumbers around 10-12 rad/m (10-11 rad/s for linear gravity waves) in waves from one storm system, rather than requiring waves from opposing storms. The existence of such wave systems is believed to be a leading mechanism through which microseismic noise is generated (Longuet-Higgins 1950; Farrell and Munk 2010; Ardhuin et al. 2015).

Our measurements provide no definitive mechanism which leads to such a wide bimodal spectrum; however, there are some suggestions in the literature. From the available four-wave numerical modeling (e.g. Dysthe et al. 2003; Socquet-Juglard et al. 2005) the broadest bimodal effects have been seen out to $\pm 70^o$. But it is important to remember that the standard gravity-wave modeling using four-wave resonance is just an asymptotic model and for larger times and larger slopes five- and higher wave resonances are possible. For example, in the laboratory Su et al. (1982) and Melville (1982) showed direct evidence of the growth of crescent-shaped waves which occur at larger wave slopes and are the result of five-wave interactions leading to three-dimensional instabilities that are stronger than the two-dimensional Benjamin-Feir instabilities (McLean et al. 1981). The tails of the crescent-shaped waves propagate in almost opposing transverse directions. Wave breaking can also be a source of wave components travelling in almost transverse directions as well as upstream (Rapp and Melville 1990). In general, breaking must be considered as an omnidirectional source of high wavenumber disturbances, but as far as we are aware there has not been any modelling of these effects. Thus the source of the opposing transverse waves remains elusive, but the evidence presented here calls for more measurements and modeling of higher-order wave-wave interactions.

The omnidirectional wavenumber spectra show a consistent power law behavior, proportional to $k^{-5/2}$ in the equilibrium range, and k^{-3} in the saturation range. The transition between these two regimes is very well defined and we find good agreement with the model of Phillips (1985) that predicts that the upper limit of the wavenumber in the equilibrium range is, to within a factor of 1-2, proportional to $(u_*^2/g)^{-1}$. The collapse across the equilibrium-saturation ranges of the omnidirectional saturation wavenumber spectra plotted against non-dimensional wavenumber $\hat{k}$ is remarkable, as shown in figure 11. Note that the same scaling is also very effective in collapsing the bimodal azimuthal separation found in the directional properties of the spectra.

Direct measurements of the transition across the equilibrium and saturation regimes, over a broad range of environmental conditions, offer an opportunity to test the empirical parameterization of k_n of Romero and Melville (2010a,b), defined as a function of the zero-up crossing wavenumber, k_u, of the azimuth-integrated non-linear energy fluxes S_{nl} based on Phillips' (1985) equilibrium argument. The upper limit of the equilibrium range is indeed a function of k_u, with a clear dependence on wave age and the non-dimensional atmospheric friction velocity $u_*/\sqrt{gH_s}$. This non-dimensional quantity appears to be better suited in the present data set to capture the evolution of the equilibrium-saturation ranges than is the wave age.

Now able to characterize its spectral bounds, we showed that the equilibrium range of the surface wave field contributed up to $10-30\%$ of the total Cox and Munk (1954) mean-square slope in our measurements.

Acknowledgments. The authors are grateful to Aspen Helicopter for providing flight resources, Barry Hansen for his excellent piloting during the SOCAL2013 flights, and Nick Statom for collecting and processing the airborne lidar data. We are thankful to Laurent Grare for providing the atmospheric data collected from R/P FLIP and for helpful discussions. We thank Luc Deike for useful comments and suggestions on the data analysis and interpretation of the lidar data, and Leonel Romero for his support with WaveWatch-III. Fabrice Veron generously shared his data for Figure 10. We are thankful to Luigi Cavaleri (ISMAR, Venice) and an anonymous reviewer for their suggestions, which improved the paper. This research was supported by grants to WKM from the Physical Oceanography programs at ONR and NSF (OCE).

References

Ardhuin, F., L. Gualtieri, and E. Stutzmann, 2015: How ocean waves rock the earth: Two mechanisms explain microseisms with periods 3 to 300 s. *Geophysical Research Letters*, **42 (3)**, 765–772.

Banner, M., I. S. Jones, and J. Trinder, 1989: Wavenumber spectra of short gravity waves. *Journal of Fluid Mechanics*, **198**, 321–344.

Banner, M., and I. Young, 1994: Modeling spectral dissipation in the evolution of wind waves. part i: Assessment of existing model performance. *Journal of physical oceanography*, **24 (7)**, 1550–1571.

Banner, M. L., 1990: Equilibrium spectra of wind waves. *Journal of physical oceanography*, **20 (7)**, 966–984.

Battjes, J. A., T. J. Zitman, and L. H. Holthuusen, 1987: A reanalysis of the spectra observed in jonswap. *Journal of Physical Oceanography*, **17 (8)**, 1288–1295.

Bréon, F., and N. Henriot, 2006: Spaceborne observations of ocean glint reflectance and modeling of wave slope distributions. *Journal of Geophysical Research: Oceans*, **111 (C6)**, doi:10.1029/2005JC003343, c06005.

Cox, C., and W. Munk, 1954: Measurement of the roughness of the sea surface from photographs of the suns glitter. *JOSA*, **44 (11)**, 838–850.

Deike, L., L. Lenain, and W. K. Melville, 2017: Air entrainment by breaking waves. *Geophysical Research Letters*, **44 (12)**, doi:10.1002/2017GL072883, URL http://dx.doi.org/10.1002/2017GL072883.

Donelan, M. A., J. Hamilton, and W. Hui, 1985: Directional spectra of wind-generated waves. *Philosophical Transactions of the Royal Society of London A: Mathematical, Physical and Engineering Sciences*, **315 (1534)**, 509–562.

Drazen, D. A., W. K. Melville, and L. Lenain, 2008: Inertial scaling of dissipation in unsteady breaking waves. *Journal of Fluid Mechanics*, **611**, 307–332.

Dysthe, K. B., K. Trulsen, H. E. Krogstad, and H. Socquet-Juglard, 2003: Evolution of a narrow-band spectrum of random surface gravity waves. *Journal of Fluid Mechanics*, **478**, 1–10.

Elfouhaily, T., B. Chapron, K. Katsaros, and D. Vandemark, 1997: A unified directional spectrum for long and short wind-driven waves. *Journal of Geophysical Research: Oceans*, **102 (C7)**, 15 781–15 796.

Farrell, W. E., and W. Munk, 2010: Booms and busts in the deep. *Journal of Physical Oceanography*, **40 (9)**, 2159–2169, doi:10.1175/2010JPO4440.1.

Forristall, G. Z., 1981: Measurements of a saturated range in ocean wave spectra. *Journal of Geophysical Research: Oceans*, **86 (C9)**, 8075–8084.

Grare, L., L. Lenain, and W. K. Melville, 2016: The influence of wind direction on campbell scientific csat3 and gill r3-50 sonic anemometer measurements. *Journal of Atmospheric and Oceanic Technology*, **33 (11)**, 2477–2497.

Hanley, K. E., S. E. Belcher, and P. P. Sullivan, 2010: A global climatology of wind–wave interaction. *Journal of Physical Oceanography*, **40 (6)**, 1263–1282.

Hwang, P. A., 2005: Wave number spectrum and mean square slope of intermediate-scale ocean surface waves. *Journal of Geophysical Research: Oceans*, **110 (C10)**, doi:10.1029/2005JC003002, c10029.

Hwang, P. A., D. W. Wang, E. J. Walsh, W. B. Krabill, and R. N. Swift, 2000a: Airborne measurements of the wavenumber spectra of ocean surface waves. part i: Spectral slope and dimensionless spectral coefficient. *Journal of Physical Oceanography*, **30 (11)**, 2753–2767.

Hwang, P. A., D. W. Wang, E. J. Walsh, W. B. Krabill, and R. N. Swift, 2000b: Airborne measurements of the wavenumber spectra of ocean surface waves. part ii: Directional distribution. *Journal of Physical Oceanography*, **30 (11)**, 2768–2787.

Jähne, B., and K. S. Riemer, 1990: Two-dimensional wave number spectra of small-scale water surface waves. *Journal of Geophysical Research: Oceans*, **95 (C7)**, 11 531–11 546.

Kahma, K. K., and C. J. Calkoen, 1992: Reconciling discrepancies in the observed growth of wind-generated waves. *Journal of Physical Oceanography*, **22 (12)**, 1389–1405.

Kitaigordskii, S., V. Krasitskii, and M. Zaslavskii, 1975: On Phillips' theory of equilibrium range in the spectra of wind-generated gravity waves. *Journal of Physical Oceanography*, **5 (3)**, 410–420.

Kitaigorodskii, S., 1962: Applications of the theory of similarity to the analysis of wind-generated wave motion as a stochastic process. *Izv. Geophys. Ser. Acad. Sci., USSR*, **1**, 105–117.

Kitaigorodskii, S., 1983: On the theory of the equilibrium range in the spectrum of wind-generated gravity waves. *Journal of Physical Oceanography*, **13 (5)**, 816–827.

Kleiss, J. M., and W. K. Melville, 2010: Observations of wave breaking kinematics in fetch-limited seas. *Journal of Physical Oceanography*, **40 (12)**, 2575–2604.

Kleiss, J. M., and W. K. Melville, 2011: The analysis of sea surface imagery for whitecap kinematics. *Journal of Atmospheric and Oceanic Technology*, **28 (2)**, 219–243.

Leckler, F., F. Ardhuin, C. Peureux, A. Benetazzo, F. Bergamasco, and V. Dulov, 2015: Analysis and interpretation of frequency–wavenumber spectra of young wind waves. *Journal of Physical Oceanography*, **45 (10)**, 2484–2496.

Long, C. E., and D. T. Resio, 2007: Wind wave spectral observations in Currituck sound, North Carolina. *Journal of Geophysical Research: Oceans*, **112 (C5)**, doi:10.1029/2006JC003835, c05001.

Longuet-Higgins, M. S., 1950: A theory of the origin of microseisms. *Philosophical Transactions of the Royal Society of London A: Mathematical, Physical and Engineering Sciences*, **243 (857)**, 1–35.

McLean, J., Y. Ma, D. Martin, P. Saffman, and H. Yuen, 1981: Three-dimensional instability of finite-amplitude water waves. *Physical Review Letters*, **46 (13)**, 817.

Melville, W., 1982: The instability and breaking of deep-water waves. *Journal of Fluid Mechanics*, **115**, 165–185.

Melville, W. K., L. Lenain, D. R. Cayan, M. Kahru, J. P. Kleissl, P. Linden, and N. M. Statom, 2016: The modular aerial sensing system. *Journal of Atmospheric and Oceanic Technology*, **33 (6)**, 1169–1184.

Melville, W. K., and P. Matusov, 2002: Distribution of breaking waves at the ocean surface. *Nature*, **417 (6884)**, 58–63.

Phillips, O. M., 1958: The equilibrium range in the spectrum of wind-generated waves. *Journal of Fluid Mechanics*, **4 (04)**, 426–434.

Phillips, O. M., 1985: Spectral and statistical properties of the equilibrium range in wind-generated gravity waves. *Journal of Fluid Mechanics*, **156**, 505–531.

Pushkarev, A., D. Resio, and V. Zakharov, 2003: Weak turbulent approach to the wind-generated gravity sea waves. *Physica D: Nonlinear Phenomena*, **184 (1)**, 29–63.

Rapp, R. J., and W. Melville, 1990: Laboratory measurements of deep-water breaking waves. *Philosophical Transactions of the Royal Society of London A: Mathematical, Physical and Engineering Sciences*, **331 (1622)**, 735–800.

Reineman, B. D., L. Lenain, D. Castel, and W. K. Melville, 2009: A portable airborne scanning lidar system for ocean and coastal applications. *Journal of Atmospheric and oceanic technology*, **26 (12)**, 2626–2641.

Resio, D. T., C. E. Long, and C. L. Vincent, 2004: Equilibrium-range constant in wind-generated wave spectra. *Journal of Geophysical Research: Oceans*, **109 (C1)**, doi:10.1029/2003JC001788, c01018.

Romero, L., and W. K. Melville, 2010a: Airborne observations of fetch-limited waves in the Gulf of Tehuantepec. *Journal of Physical Oceanography*, **40 (3)**, 441–465.

Romero, L., and W. K. Melville, 2010b: Numerical modeling of fetch-limited waves in the Gulf of Tehuantepec. *Journal of Physical Oceanography*, **40 (3)**, 466–486.

Romero, L., W. K. Melville, and J. M. Kleiss, 2012: Spectral energy dissipation due to surface wave breaking. *Journal of Physical Oceanography*, **42 (9)**, 1421–1444.

Socquet-Juglard, H., K. Dysthe, K. Trulsen, H. E. Krogstad, and J. Liu, 2005: Probability distributions of surface gravity waves during spectral changes. *Journal of Fluid Mechanics*, **542**, 195–216.

Su, M.-Y., M. Bergin, P. Marler, and R. Myrick, 1982: Experiments on non-linear instabilities and evolution of steep gravity-wave trains. *Journal of Fluid Mechanics*, **124 (1)**, 45.

Sutherland, P., and W. K. Melville, 2013: Field measurements and scaling of ocean surface wave-breaking statistics. *Geophysical Research Letters*, **40 (12)**, 3074–3079, doi:10.1002/grl.50584, URL http://dx.doi.org/10.1002/grl.50584.

Toba, Y., 1973: Local balance in the air-sea boundary processes. *Journal of the Oceanographical Society of Japan*, **29 (5)**, 209–220.

Tracy, B. A., and D. T. Resio, 1982: Theory and calculation of the nonlinear energy transfer between sea waves in deep water. Tech. rep., WIS Technical Report 11, US Army Engineer Waterways Experiment Station, Vicksburg, MS, USA.

van Vledder, G. P., 2006: The wrt method for the computation of non-linear four-wave interactions in discrete spectral wave models. *Coastal Engineering*, **53 (2)**, 223–242.

Walsh, E., D. Hancock III, D. Hines, R. Swift, and J. Scott, 1985: Directional wave spectra measured with the surface contour radar. *Journal of physical oceanography*, **15 (5)**, 566–592.

Webb, D., 1978: Non-linear transfers between sea waves. *Deep Sea Research*, **25 (3)**, 279–298.

Young, I., 2010: The form of the asymptotic depth-limited wind-wave spectrum: Part III Directional spreading. *Coastal Engineering*, **57 (1)**, 30–40.

Yurovskaya, M., V. Dulov, B. Chapron, and V. Kudryavtsev, 2013: Directional short wind wave spectra derived from the sea surface photography. *Journal of Geophysical Research: Oceans*, **118 (9)**, 4380–4394.

Zakharov, V., and N. Filonenko, 1967: Energy spectrum for stochastic oscillations of the surface of a liquid. *Soviet Physics Doklady*, Vol. 11, 881.

Zappa, C. J., M. L. Banner, H. Schultz, A. Corrada-Emmanuel, L. B. Wolff, and J. Yalcin, 2008: Retrieval of short ocean wave slope using polarimetric imaging. *Measurement Science and Technology*, **19 (5)**, 055 503.

LIST OF TABLES

$k\ (rad/m)$	0.01	0.05	0.1	0.5	1	10
$d\theta\ (rad)$	6.2	1.24	0.62	0.124	0.062	0.0062

TABLE 1: Directional resolution for selected wavenumbers.

LIST OF FIGURES

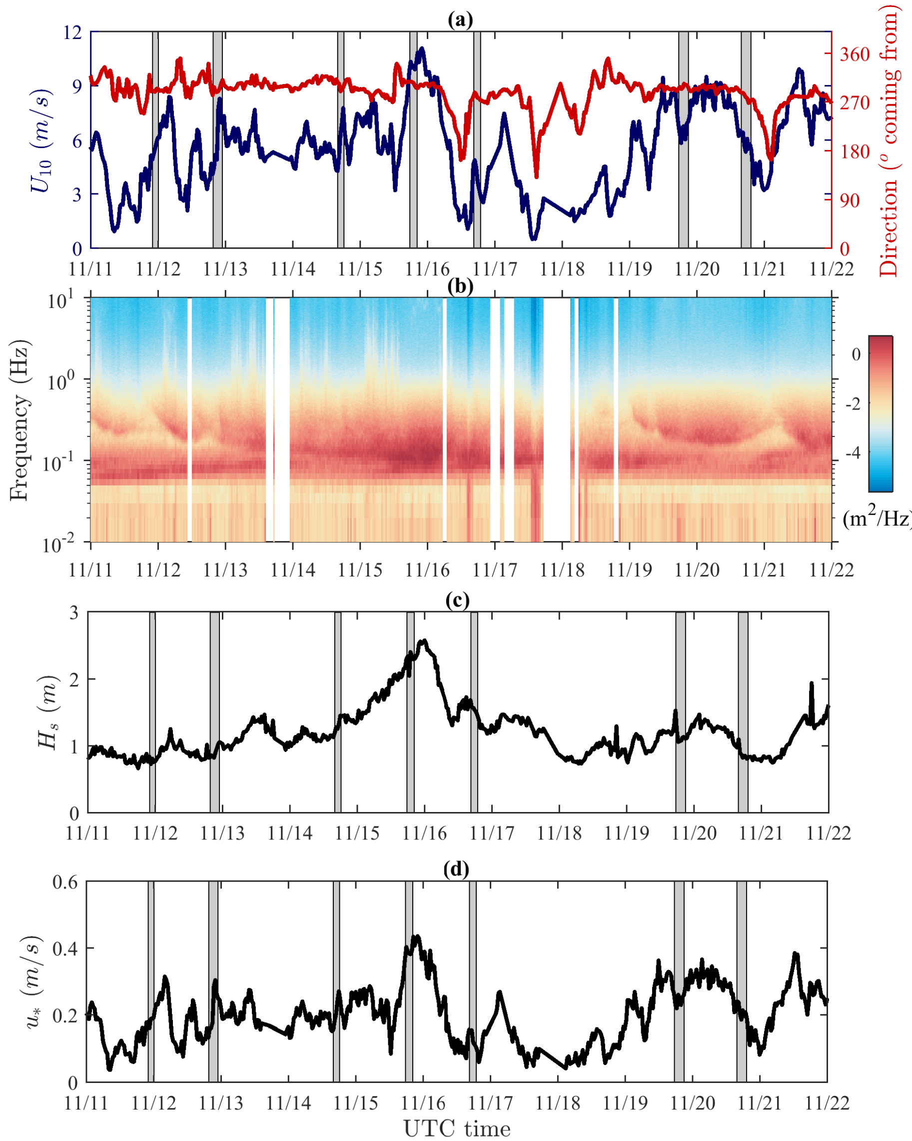

FIG. 1: Environmental conditions collected from R/P FLIP during the SOCAL2013 Experiment: (a) U_{10} (dark blue line), wind direction (red line), (b) spectrogram of the surface displacement, (c) significant wave height H_s and (d) atmospheric friction velocity u_*. All data points are 30-min averages. The thick gray vertical lines represent the periods of time when the aircraft was on station.

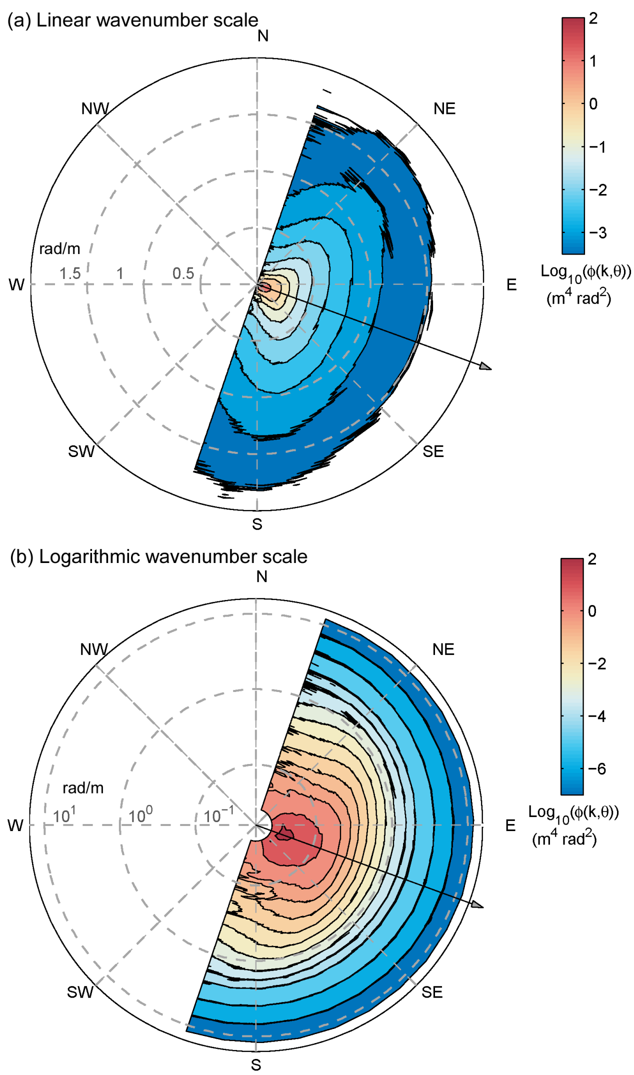

FIG. 2: Sample directional wavenumber spectrum $\phi(k, \theta)$ collected on November 15 2013 during the SOCAL2013 experiment,(a) using a linear scale for the wavenumber k (rad/m), and (b) in logscale. Note the clear bimodal distribution, particularly evident in (a). The arrow represents the direction the waves at the peak wavenumber are *propagating*. The average wind speed U_{10}, collected on R/P FLIP, was equal to 10.2 m/s at the time of the flight. Note that for clarity, only a portion of the data, up to 1.5-2 rad/m, are shown in (a).

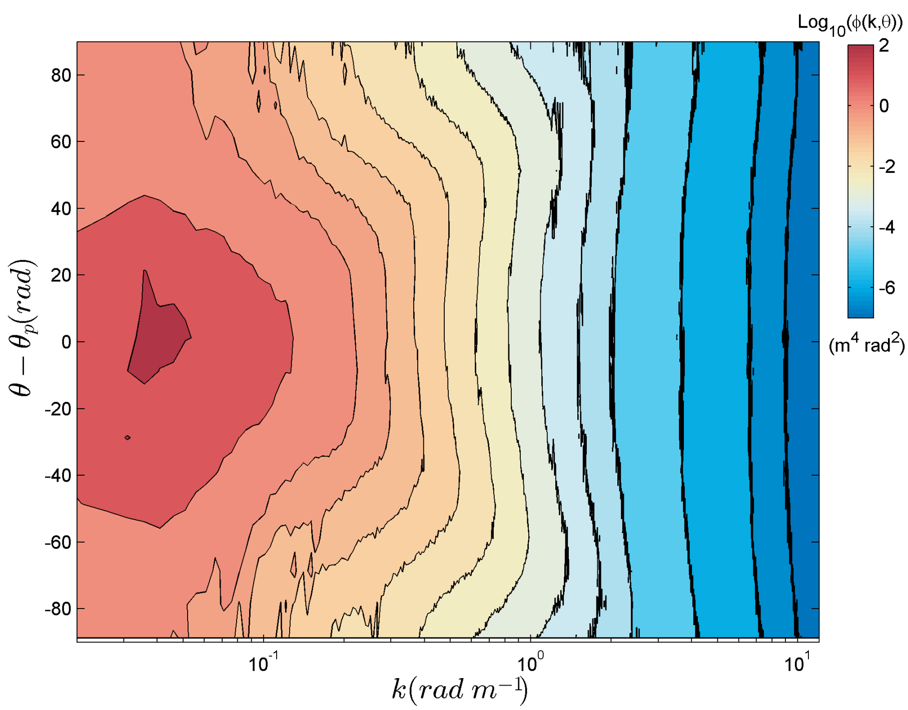

FIG. 3: The same directional wavenumber spectrum $\phi(k,\theta)$ shown in figure 2 collected on November 15 2013 during the SOCAL2013 experiment, plotted against k and relative azimuthal direction $\theta - \theta_p$. Note the clear bimodal distribution extending up to the larger values of k. An isotropic spectrum would be depicted as a vertical contour line.

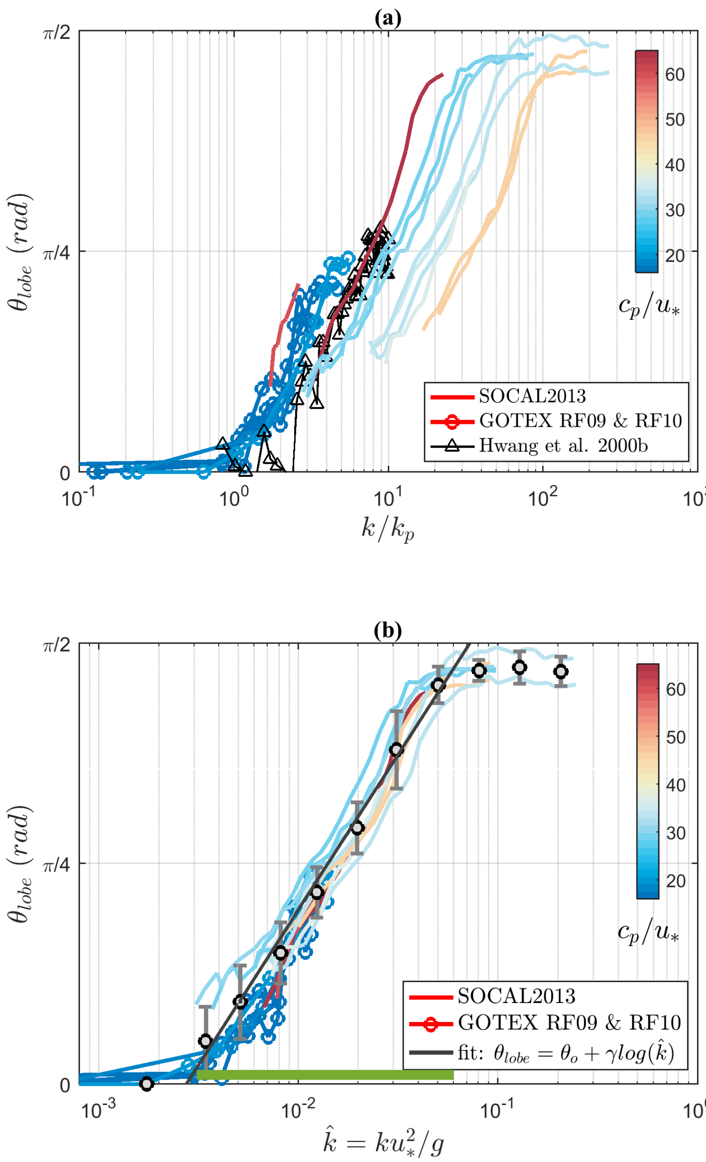

FIG. 4: Bin averaged lobe separation θ_{lobe} plotted against (a) normalized wavenumber k/k_p and (b) non dimensional ku_*^2/g, colorcoded for wave age c_p/u_* for the SOCAL2013 (solid line) and GOTEX (solid line with circle) experiments. RF09 and RF10 represent two of the research flights conducted during GOTEX (Romero and Melville 2010a). The black open triangle corresponds to the measurements by Hwang et al. (2000b). A power fit is also shown in (b), along with bin-averaged values of the lobe separation computed over the SOCAL2013 and GOTEX data sets (black circles) and corresponding error bars (one standard deviation). We find $r^2 = 0.96$ for the fit with $\theta_0 = 2.835$ and $\gamma = 0.48$. The range of validity of the fit is represented as a green horizontal bar.

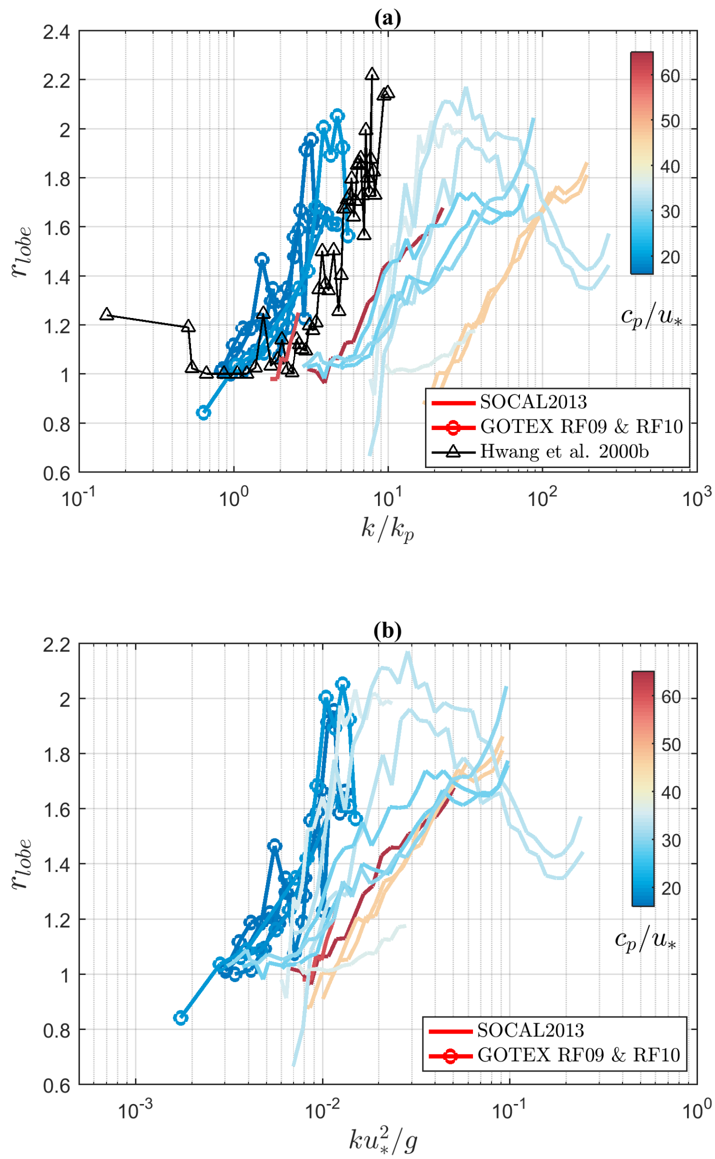

FIG. 5: Bin averaged relative lobe amplitude r_{lobe} plotted against (a) normalized wavenumber k/k_p and (b) non dimensional ku_*^2/g, colorcoded for wave age c_p/u_* for the SOCAL2013 (solid line) and GOTEX (solid line with circle) experiments. The black open triangle corresponds to the measurements by Hwang et al. (2000b).

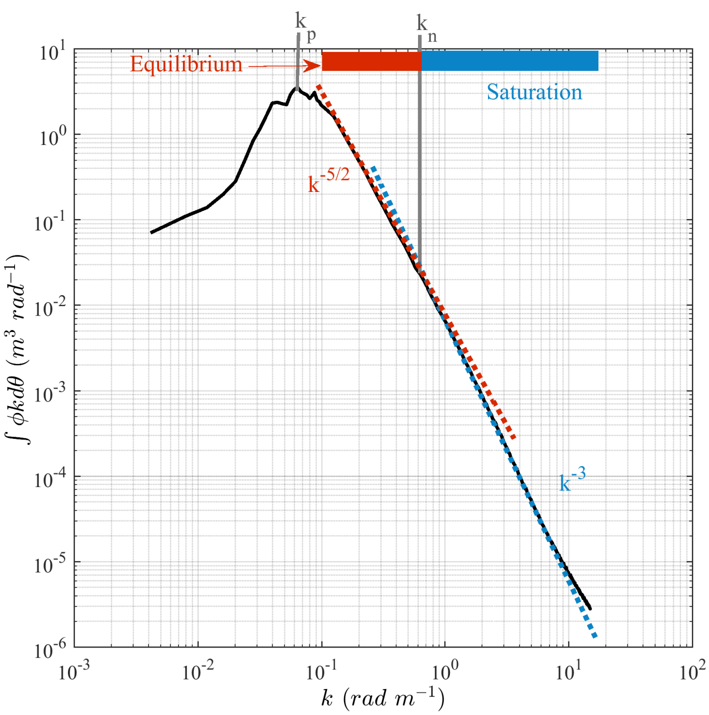

FIG. 6: Sample omnidirectional wavenumber spectrum collected on November 15 2013 during the SOCAL2013 experiment. Note the -5/2 and -3 spectral slopes, and the three-decade bandwidth of the data.

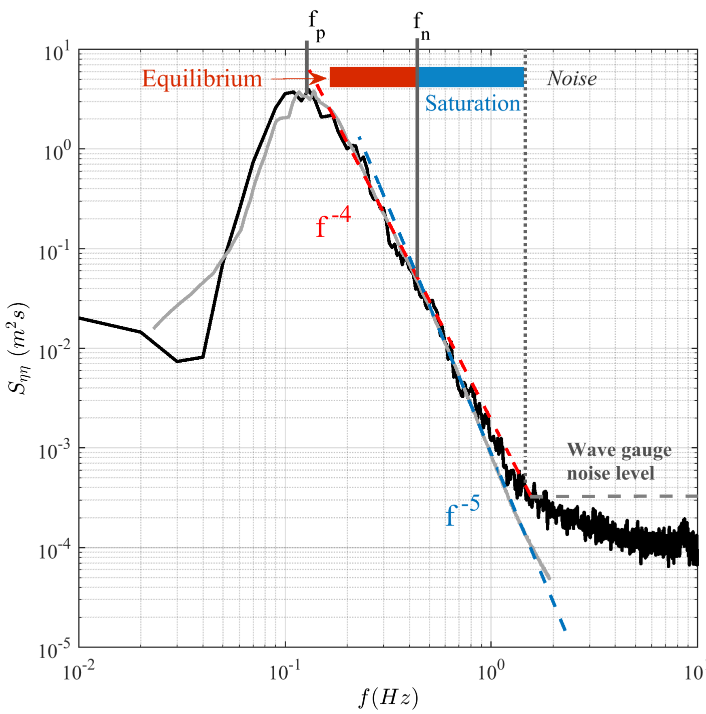

FIG. 7: Wave frequency spectrum (black) computed from wave gauge installed on one of R/P FLIP's booms at the time when the airborne lidar data shown in figure 6 were collected, on November 15 2015, along with the frequency spectrum (using the linear dispersion relationship) computed from the directional wavenumber spectrum (gray) used to generate figure 6. Also shown are the saturation and equilibrium ranges, determined from the wavenumber spectrum. While obvious in figure 6, and in its frequency spectrum equivalent, the transition from a f^{-4} to f^{-5} behavior is not discernable in the frequency spectrum computed from the laser wave gauge on FLIP.

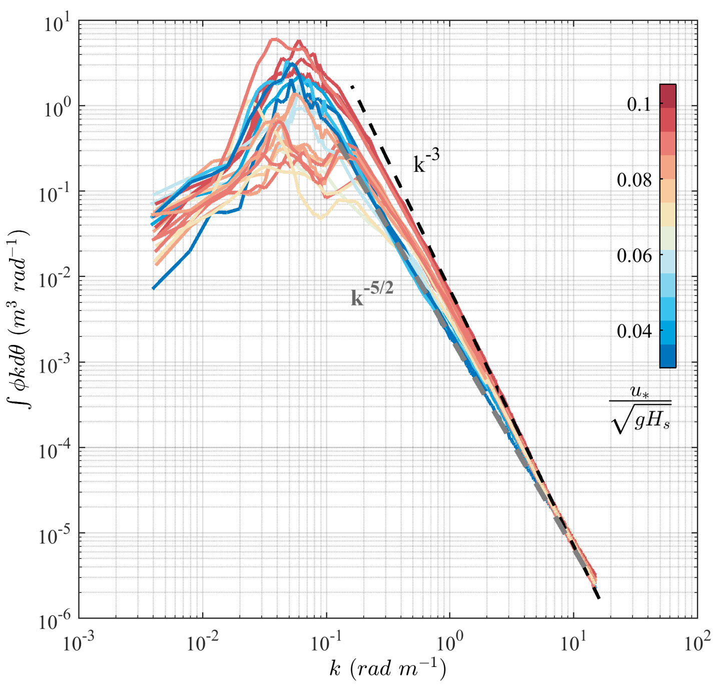

FIG. 8: Omnidirectional spectra collected during the SOCAL2013 experiment, colorcoded for the ratio $\frac{u_*}{\sqrt{gH_s}}$.

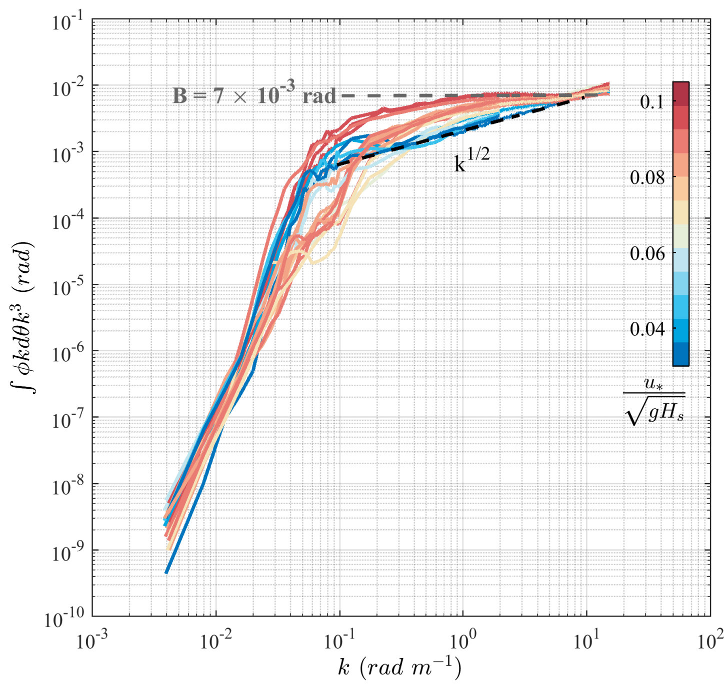

FIG. 9: Azimuth-integrated saturation spectra $B(k) = \int \phi k^4 d\theta$, collected during the SOCAL2013 experiment; the curves are colorcoded for the the ratio $\frac{u_*}{\sqrt{gH_s}}$.

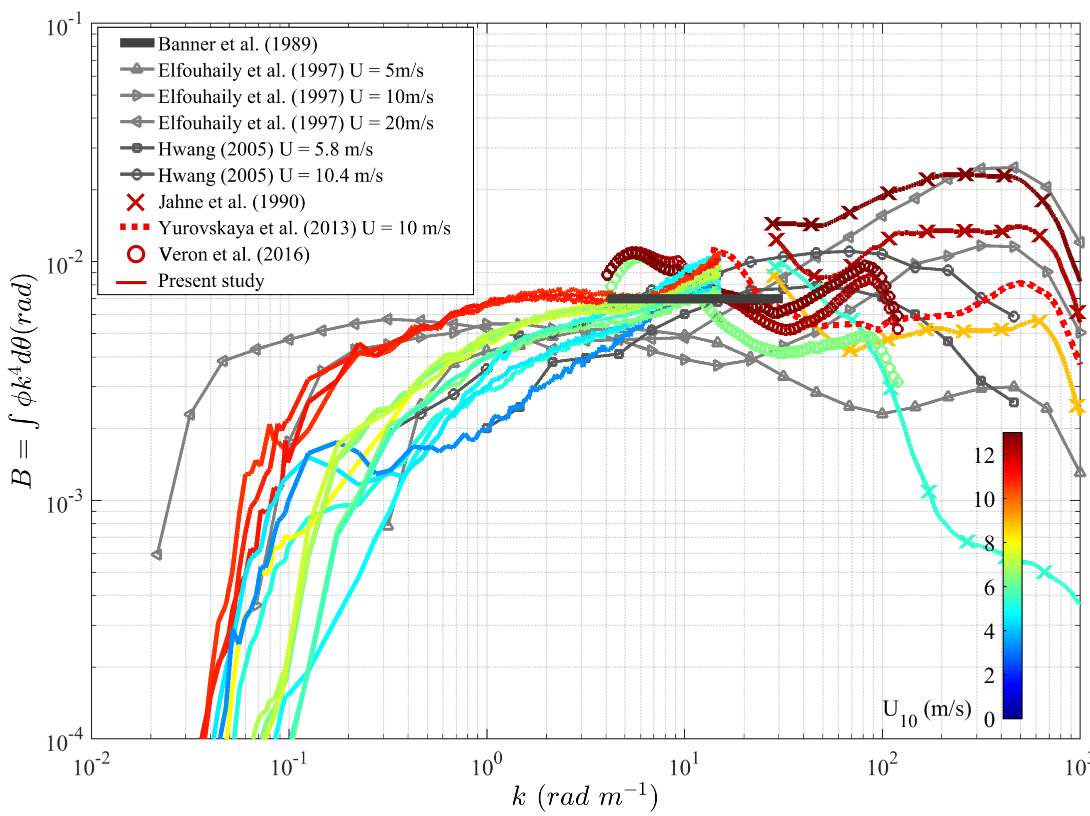

FIG. 10: Azimuth-integrated saturation spectra $B(k) = \int \phi k^4 d\theta$, collected during the SOCAL2013 experiment (solid lines) color-coded for the wind speed U_{10} along with results from past observational and modelling studies.

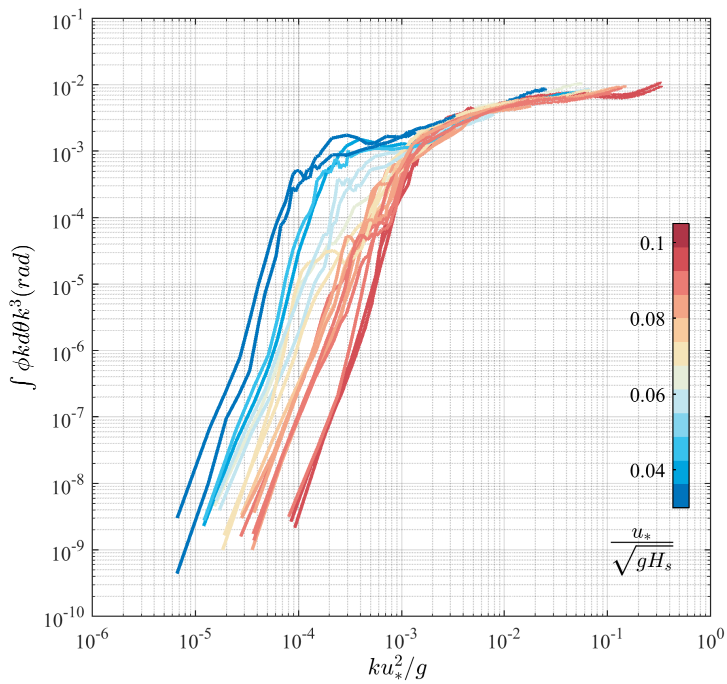

FIG. 11: Azimuth-integrated saturation spectra $B(k) = \int \phi k^4 d\theta$ plotted against $\hat{k} = ku_*^2/g$. The curves are colorcoded for the the ratio $\frac{u_*}{\sqrt{gH_s}}$. Note the collapse of the spectra for the larger values of $\hat{k}$.

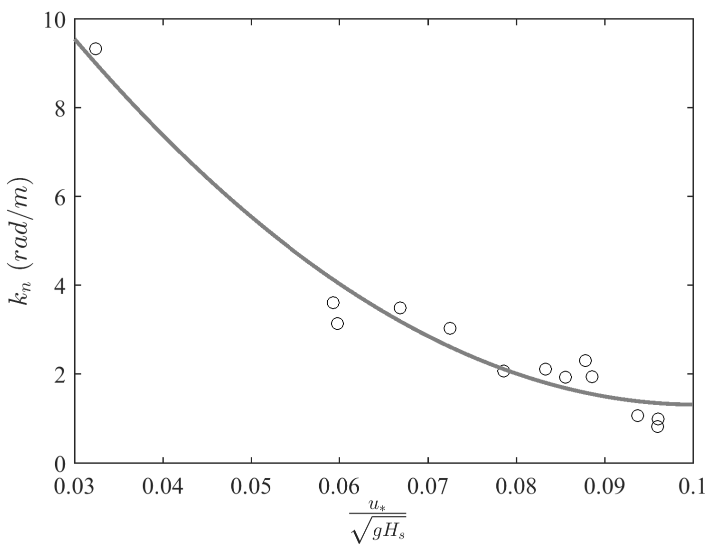

FIG. 12: The transition wavenumber k_n plotted against $\frac{u_*}{\sqrt{gH_s}}$.

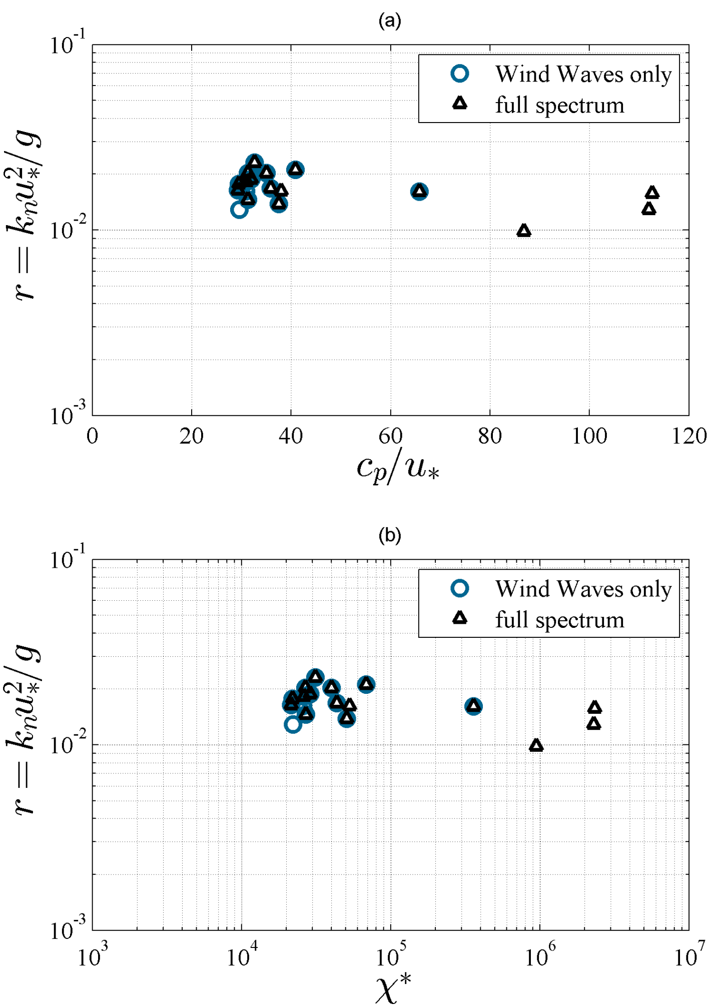

FIG. 13: The nondimensional transition wavenumber $k_n u_*^2/g$ plotted versus wave age c_p/u_* and the non-dimensional fetch χ^*.

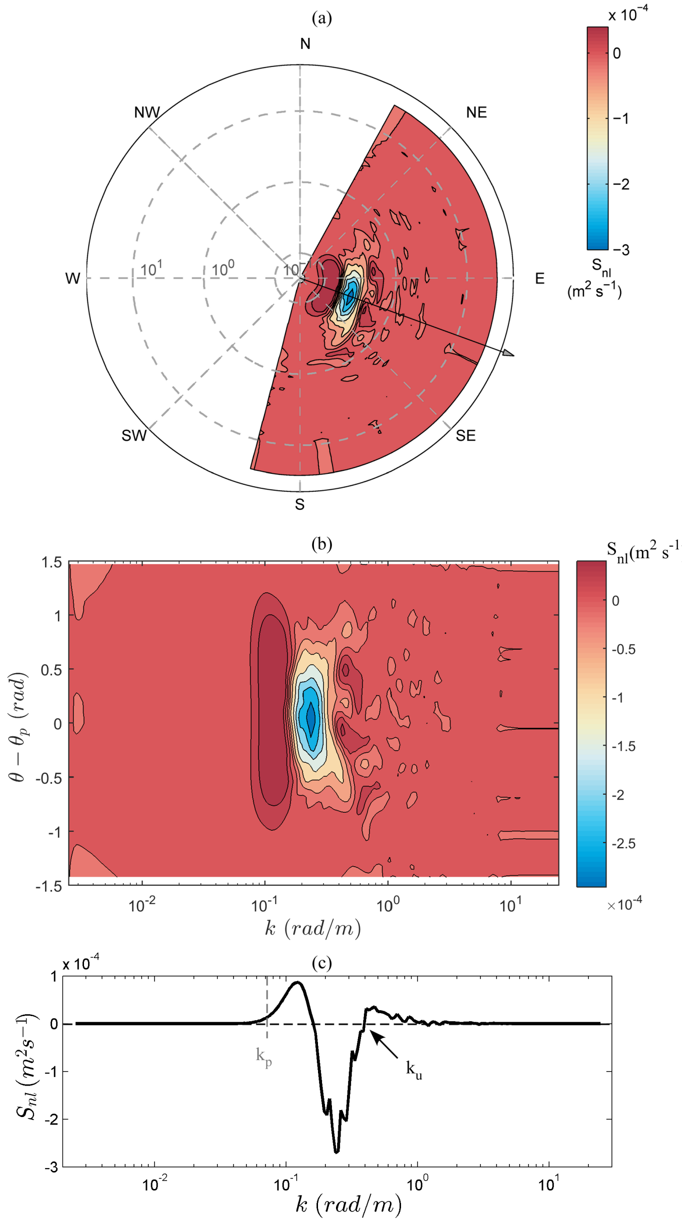

FIG. 14: Non-linear term S_{nl} of the radiative transport equation computed from the directional wavenumber spectrum shown in figure 2 displayed in polar coordinates in (a) and plotted against k and $\theta - \theta_p$ in (b). (c) Cut through along the black arrow in (a), depicting the peak wave direction (going to). The zero-up crossing wavenumber k_u is highlighted in (c).

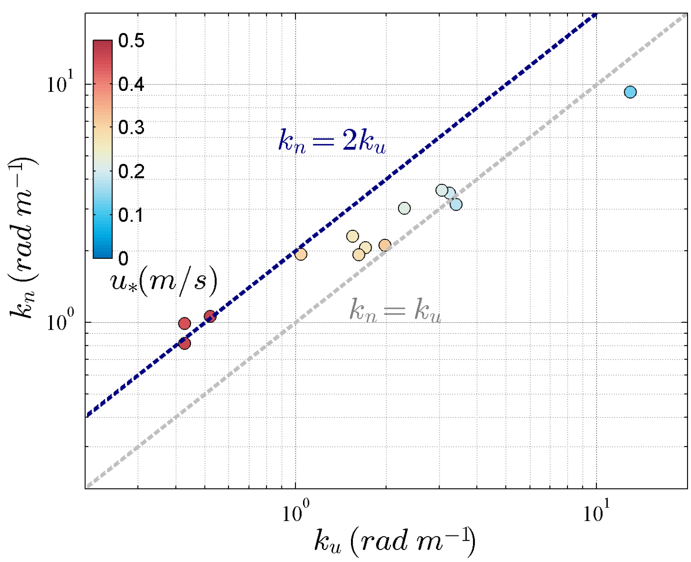

FIG. 15: Measured upper limit of the equilibrium range k_n as a function of the zero-up crossing of the non-linear energy fluxes k_u. Each point is colorcoded for friction velocity u_*.

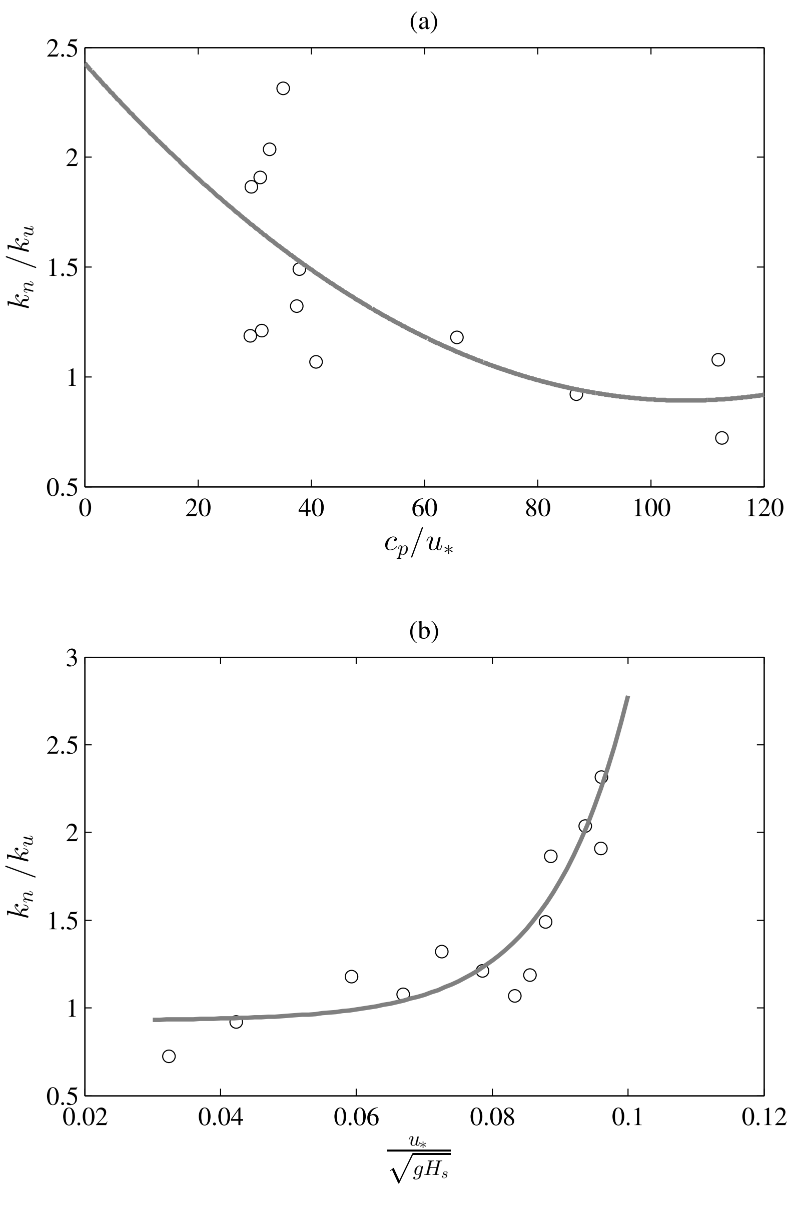

FIG. 16: Ratio k_n/k_u plotted against (a) wave age and (b) $\frac{u_*}{\sqrt{gH_s}}$. The gray curve shows the corresponding fits (r^2= 0.45 and 0.84 for (a) and (b), respectively).

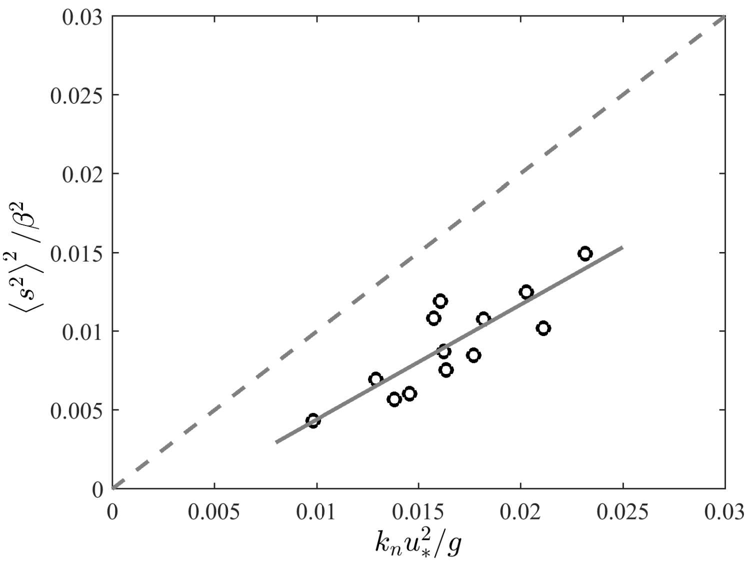

FIG. 17: Total mean squared slope squared, computed over the equilibrium range k_o to k_n, normalized by the Toba parameter (Romero and Melville 2010a) against normalized wavenumber $k_n u_*^2/g$, following Phillips (1985). A linear fit is shown in gray, where $\langle s^2 \rangle^2 / \beta^2 = 0.73\hat{k} - 0.0029$.

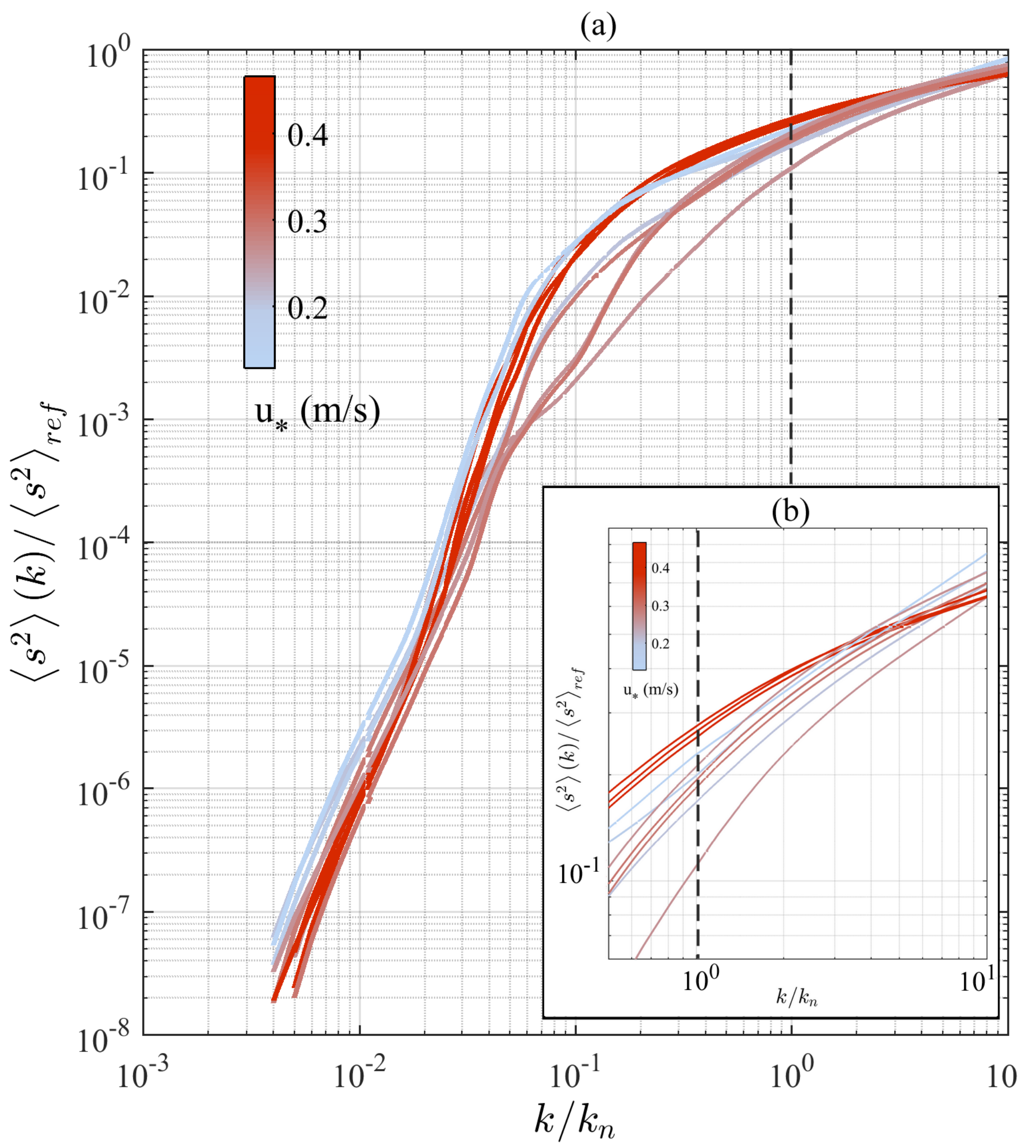

FIG. 18: (a) Total spectral mean-square slope $\langle s^2 \rangle (k)$ computed from the omnidirectional wave spectrum, normalized by the total mean-square slope defined by Cox and Munk (1954), $\langle s^2 \rangle_{ref}$, plotted against the normalized wavenumber k/k_n. (b) shows a zoomed-in version of the same plot, focusing on the higher wavenumber portion. The normalized wavenumber reference band $k/k_n = 1$ is shown as a black dashed line.